

SiFo: Wireless Foundation Model for Low-Overhead Site-Specific CSI Feedback

Cheng-Jie Zhao *Graduate Student Member, IEEE*, Zhaolin Wang, *Member, IEEE*,
Zongyao Zhao, *Member, IEEE*, and Yuanwei Liu, *Fellow, IEEE*

Abstract—SiFo, a wireless foundation model-based framework, is proposed for low-overhead site-specific channel state information (CSI) feedback. In 3GPP NR, Type-II feedback provides an expressive codebook-based CSI representation, but it requires substantial reference-signal overhead, UE-side search, and feedback. Learning-based site-specific feedback can reduce these online costs while retaining high-quality subspace representation by exploiting deployment-dependent propagation structure. However, existing site-specific designs typically train a dedicated neural network for each new site, which limits scalability when the number of deployments is large. SiFo addresses this scalability issue by pretraining a CSI feedback model across source sites and adapting it to a target site through lightweight calibration. A small set of target-site users reports low-dimensional reference signal received power (RSRP) fingerprints, and their full-CSI-based subspace labels are stored as calibration memory. During online operation, a served user is matched to calibrated users through the same SSB probing and RSRP reporting procedure, so nearby calibration samples provide site-specific subspace guidance without updating model parameters. SiFo therefore transfers common propagation knowledge while retaining local adaptation. Numerical results across ten city scenarios demonstrate that SiFo (i) achieves higher CSI-capture efficiency than separately trained site-specific learning baselines under the same target-site labeled budget, (ii) approaches the high-overhead 3GPP NR Type-II feedback reference using only RSRP measurements collected during online SSB probing, and (iii) converts the high CSI-capture efficiency and low overhead into effective spectral efficiency improvement under limited target-site data.

Index Terms—Limited CSI feedback, site-specific beamforming, wireless foundation models

I. INTRODUCTION

WIRELESS foundation models are being developed as general-purpose backbones for learning-enabled wireless systems. This direction is driven by the increasing use of learning-based modules in a wide range of wireless applications, e.g., channel acquisition, beam management, and network orchestration. In practical deployments, these modules are expected to operate across heterogeneous carrier bands, antenna arrays, protocol configurations, and propagation environments. Such heterogeneity exposes a scalability limitation of independently trained models, because labeled channel-data collection, model retraining, and deployment-specific validation may need to be repeated whenever the radio environment changes. Wireless foundation models therefore shift the design emphasis from isolated task- or site-specific learners toward reusable wireless representations that can be specialized to

new deployments with limited additional data.

In the broad sense of [1], a foundation model is pretrained on large and diverse data and can later be adapted efficiently to downstream environments or tasks. Existing wireless foundation model studies have explored this principle first from network intelligence and channel modeling perspectives. The authors of [2] proposed WirelessLLM, which exploits large language models for wireless intelligence and network orchestration. A space-time-frequency wireless foundation model, named WiFo, was developed in [3] for transferable channel prediction. The large wireless model in [4] learned contextualized channel embeddings for downstream communication and sensing tasks. For multi-task wireless communication and sensing, the authors of [5] introduced WirelessGPT through generative pretraining, and [6] further extended wireless foundation models to multi-task prediction.

Another line of work moves foundation modeling closer to physical-layer signal representations and protocol-relevant tasks. To support sensing, communication, and localization, [7] proposed WavesFM as a multi-modal wireless foundation model. From the spectrum-management perspective, SpectrumFM was developed in [8] to learn transferable spectrum representations. At the signal-representation level, the authors of [9] introduced IQFM, which learns reusable encoders directly from raw multi-antenna IQ streams. As a further step toward CSI feedback, [10] proposed WiFo-CF, a foundation model tailored to heterogeneous channel dimensions, feedback rates, and data distributions. These studies demonstrate the potential of pretraining and transfer across network-level intelligence, channel prediction, and signal representation, spectrum management. How to use a wireless foundation model for low-overhead, protocol-constrained, and limited-feedback CSI acquisition remains less explored.

Low-overhead limited-feedback CSI acquisition has traditionally been handled through structured codebook-based schemes [11], [12]. In the 3rd Generation Partnership Project (3GPP) New Radio (NR) framework, Type-I, Type-II, and enhanced Type-II port-selection codebook (PSC) schemes are representative limited-feedback options [13]. Type-I has low feedback overhead but limited single-beam representation capability in rich multipath channels. Type-II provides the most expressive multi-beam representation over an oversampled angular dictionary, but its gain comes with heavier RS acquisition, user equipment (UE)-side search, and feedback processing. PSC provides a structured alternative, yet its representation capability remains constrained by the selected port domain. Together, these schemes expose the fundamental trade-off between affordable overhead and high-quality chan-

The authors are with Department of Electrical and Computer Engineering, The University of Hong Kong, Hong Kong (e-mail: chengjie_zhao@connect.hku.hk, zhaolin.wang@hku.hk, zongyao@hku.hk, yuanwei@hku.hk).

nel representation.

Learning-based methods have been explored to improve the tradeoff among overhead, complexity, and performance. Early studies enhanced conventional beam-management and feedback procedures through learned codebooks. The authors of [14] developed machine-learning-based codebooks for NR initial access and CSI Type-II feedback, and later extended this idea to neural codebook design for broader multiple-input multiple-output (MIMO) beam-management tasks [15]. More recent works moved beyond generic codebook learning by exploiting site-specific propagation structure, including site-specific probing, RSRP-based codebook design, and channel knowledge maps [16]–[19]. In particular, site-specific beam-forming (SSBF) frameworks showed that coarse power fingerprints can be used to synthesize site-conditioned beams [20]–[22], while site-specific Type-II (SST2) feedback incorporated *site-specific information (SSI)* into the conventional Type-II (Conv-T2) feedback pipeline to reduce online overhead and UE complexity without sacrificing the expressive Type-II representation [23]. Together, these studies demonstrate the value of learning from the deployment environment. However, when such methods are extended to large-scale network deployment, their site-dependent training process becomes difficult to scale: a dedicated neural model may need to be trained and validated for each new site, and modern wireless networks may contain a very large number of deployment sites.

This scalability issue motivates a closer connection between wireless foundation models and site-specific learning. At first glance, the two directions appear to pursue opposite design philosophies: wireless foundation models emphasize reusable structures shared across tasks and deployments, whereas site-specific learning emphasizes adaptation to localized radio propagation for site-specific performance. These two goals can be made compatible if the feedback rule is decomposed into a reusable cross-site component and a lightweight site-conditioned component. Cross-site pretraining can learn common beam-domain sensing and subspace priors, while target-site calibration can supply the local propagation evidence that is not transferable across sites. The desired design is therefore neither a purely site-agnostic model nor a separately trained model for every site.

This paper studies foundation model-based site-specific CSI feedback in the Type-II setting. Type-II feedback is chosen because it provides the most expressive NR codebook-based CSI representation, and hence exposes the key difficulty of inferring a phase-aware CSI subspace from low-dimensional RSRP observations. The RSRP fingerprint contains only coarse amplitude information, whereas the desired subspace depends on multipath geometry, angular spread, phase, and scattering structure. Therefore, similar RSRP observations may correspond to different subspace decisions in different deployment sites. Direct cross-site pretraining provides a useful marginal prior, but it does not by itself recover the target-site relation from RSRP fingerprints to CSI subspaces.

Based on these observations, this paper proposes SiFo, a calibration-aided wireless foundation model design for low-overhead site-specific CSI feedback. The pretrained model provides a shared SSB probing codebook and a parametric

subspace prior, while the target site is represented by a small calibration memory. Each calibrated UE is associated with an RSRP fingerprint and an offline full-CSI-based projector. During online operation, nearby calibrated UEs in the pre-trained RSRP space provide local subspace evidence for the served UE, enabling target-site specialization without updating model parameters. The main contributions are summarized as follows:

- We establish a foundation-model view of site-specific CSI feedback. In the Type-II setting, this formulation identifies the uncertainty in inferring CSI subspaces from RSRP fingerprints as the main obstacle to direct cross-site transfer and motivates SiFo as a combination of cross-site pretraining, target-site calibration, and online subspace retrieval.
- We develop a target-site calibration principle for low-overhead CSI acquisition. The analysis shows that RSRP sensing during SSB probing should provide discriminative directional-power fingerprints, while offline full-CSI-based projector labels supply the phase-aware subspace information missing from RSRP measurements.
- We design a projector-based acquisition rule for gradient-free target-site specialization. Online UEs are matched to calibrated UEs in the pretrained RSRP coordinates, and retrieved projectors are averaged and fused with the parametric predictor to produce the prescribed rank- Q CSI representation subspace.
- We demonstrate the data and overhead efficiency of SiFo through ten-city simulations. Without target-site fine-tuning, SiFo outperforms single-site SST2 baselines under identical target-site data budgets, approaches the high-overhead Conv-T2 reference with much lower online interaction, and converts CSI-capture gains into effective-rate improvement.

The rest of this paper is organized as follows. Section II presents the system model. Section III formulates SiFo. Sections IV and V develop calibration and projector-memory acquisition. Section VI gives the deployment protocol. Section VII reports simulations, and Section VIII concludes the paper.

Notation: Scalars, vectors, matrices, and sets are denoted by italic, boldface lowercase, boldface uppercase, and calligraphic letters, respectively. \mathbb{C} and \mathbb{R} denote the complex and real fields. $(\cdot)^T$ and $(\cdot)^H$ denote transpose and Hermitian transpose. For vectors, $\|\cdot\|_2$ denotes the Euclidean norm. For matrices, $\|\cdot\|_2$ and $\|\cdot\|_F$ denote the spectral and Frobenius norms. $\text{span}(\cdot)$ denotes column space, \mathbf{I}_N is the $N \times N$ identity matrix, and $\text{tr}(\cdot)$, $\text{diag}(\cdot)$, and $\text{rank}(\cdot)$ denote trace, diagonal vector, and rank. $\mathbb{E}[\cdot]$ denotes expectation, and $\mathcal{CN}(\boldsymbol{\mu}, \boldsymbol{\Sigma})$ denotes the circularly symmetric complex Gaussian distribution.

II. SYSTEM MODEL AND PROBLEM FORMULATION

We consider a single-cell downlink communication system, where a BS equipped with N_t transmit antennas serves UEs deployed in a site indexed by s . The channel distribution is determined by the radio propagation environments and therefore varies significantly across different sites. For each

site, the channel is assumed to be block-fading, i.e., approximately constant within one coherence interval, during which SSB probing, CSI-RS transmission, and UE feedback are performed, followed by data transmission.

A. Channel and Signal Model

The BS is assumed to employ a uniform linear array (ULA) with inter-element spacing d . We adopt the standard narrowband geometric channel model, where the channel is represented as a superposition of several dominant propagation paths [24]. For UE q in site s , the channel vector can be expressed as follows

$$\mathbf{h}_{s,q} = \sum_{\ell=1}^{L_{s,q}} \alpha_{s,q,\ell} \mathbf{a}(u_{s,q,\ell}) = \mathbf{A}_{s,q} \boldsymbol{\alpha}_{s,q} \in \mathbb{C}^{N_t \times 1}, \quad (1)$$

where $L_{s,q}$ is the number of propagation paths, $\alpha_{s,q,\ell} \in \mathbb{C}$ is the complex path gain of the ℓ -th path, and $\mathbf{a}(u_{s,q,\ell})$ is the corresponding normalized steering vector. For a ULA, the steering vector is given by

$$\mathbf{a}(u) = \frac{1}{\sqrt{N_t}} \left[1, e^{j2\pi u}, \dots, e^{j2\pi(N_t-1)u} \right]^T \in \mathbb{C}^{N_t \times 1}, \quad (2)$$

where u is the spatial frequency. Specifically, for the ℓ -th path of UE q in site s , we define $u_{s,q,\ell} \triangleq d \sin(\varphi_{s,q,\ell})/\lambda$, where λ is the carrier wavelength, and $\varphi_{s,q,\ell}$ is the angle of departure (AoD) from the BS to UE q . In addition, $\mathbf{A}_{s,q} = [\mathbf{a}(u_{s,q,1}), \dots, \mathbf{a}(u_{s,q,L_{s,q}})] \in \mathbb{C}^{N_t \times L_{s,q}}$ and $\boldsymbol{\alpha}_{s,q} = [\alpha_{s,q,1}, \dots, \alpha_{s,q,L_{s,q}}]^T \in \mathbb{C}^{L_{s,q} \times 1}$ collect the steering vectors and path gains, respectively.

Assumption 1 (*Near-orthogonal angular paths*). The UE lies in the far field of the BS array, and the dominant path spatial frequencies $\{u_{s,q,\ell}\}_{\ell=1}^{L_{s,q}}$ are sufficiently separated relative to the array aperture. Therefore, the steering vectors of the dominant paths are approximately orthogonal, i.e.,

$$\mathbf{A}_{s,q}^H \mathbf{A}_{s,q} \approx \mathbf{I}_{L_{s,q}}. \quad (3)$$

This approximation is consistent with the favorable-propagation behavior of large antenna arrays with resolvable angular paths [25], [26].

Let $\mathbf{w} \in \mathbb{C}^{N_t \times 1}$ and x denote the unit-power beamformer and symbol transmitted by the BS, respectively. Then, the received signal at the UE q in site s is given by

$$y = \sqrt{P_s} \mathbf{h}_{s,q}^H \mathbf{w} x + n, \quad (4)$$

where P_s is the transmit power at site s , and $n \sim \mathcal{CN}(0, \sigma_{n,s}^2)$ is additive noise independent of the transmitted signal.

B. Beam Alignment Procedure

In practical NR systems, beam alignment refers broadly to the procedure of identifying suitable beam directions or a low-dimensional beam-space representation for subsequent CSI acquisition and downlink transmission [13], [27]–[29]. The procedure typically starts with SSB beam sweeping, where the BS transmits a predefined set of synchronization beams $\mathcal{B}_s = \{\mathbf{b}_{s,k}\}_{k=1}^K$, and the UE measures their RSRP fingerprint

$\mathbf{r}_{s,q}(\mathbf{B}_s)$ for initial access and coarse directional acquisition¹. $\mathbf{B}_s = [\mathbf{b}_{s,1}, \dots, \mathbf{b}_{s,K}]$ is a matrix collecting the SSB beams. The number of SSB beams K is assumed fixed across sites, while their beam coefficients can vary across different site to adapt to the deployment environment [22].

The SSB transmission follows the model in (4), where \mathbf{w} is specified as the SSB beams in \mathbf{B}_s and x denotes the transmitted SSB symbol. For each SSB beam, the UE averages the received signal power over the corresponding time-frequency SSB resources. The resulting RSRP value is therefore a beam-domain power measurement. Collecting the K measurements over all SSB beams gives the RSRP fingerprint $\mathbf{r}_{s,q}(\mathbf{B}_s)$, which is reported by UE q in a decibel (dB) form. Following [22], the dB-domain RSRP fingerprint can be modeled as

$$\mathbf{r}_{s,q}(\mathbf{B}_s) = \mathcal{M}(\mathbf{h}_{s,q}, \mathbf{B}_s) + \mathbf{n}_{s,q} = \bar{\mathbf{r}}_{s,q}(\mathbf{B}_s) + \mathbf{n}_{s,q}, \quad (5)$$

where $\mathcal{M}(\cdot)$ denotes the RSRP measurement operator, $\bar{\mathbf{r}}_{s,q}(\mathbf{B}_s)$ is the noise-free RSRP, and $\mathbf{n}_{s,q}$ collects Gaussian noise. The detailed expressions of $\bar{\mathbf{r}}_{s,q}(\mathbf{B}_s)$ and $\mathbf{n}_{s,q}$ are given in Section II of [22].

The RSRP fingerprint obtained at the SSB stage provides only coarse beam-level observations and is generally insufficient for high-resolution downlink precoding. To support data transmission, the system usually proceeds to a CSI refinement stage with three steps [13], [27], [28]: 1) the BS transmits CSI-RS on configured CSI-RS resources, 2) the UE estimates the downlink channel representation from the CSI-RS measurements, and 3) instead of feeding back the full channel vector, the UE reports a finite-dimensional CSI description, e.g., codebook indices, selected subspace, or low-dimensional coefficients, to support the BS's final beamforming decision due to limited channel resources. According to the analysis in [23], the effect of such a limited-feedback rule can be represented by the spatial subspace used for CSI-RS precoding. For a feedback rule ψ , let $\mathbf{U}_{s,q}^{(\psi)}$ denote the selected subspace basis vectors produced for UE q in site s . The corresponding representing subspace is

$$\mathcal{U}_{s,q}^{(\psi)} \triangleq \text{span}(\mathbf{U}_{s,q}^{(\psi)}). \quad (6)$$

Assuming that $\mathbf{U}_{s,q}^{(\psi)}$ has full column rank, the orthogonal projector onto this subspace is given by

$$\mathbf{P}_{s,q}^{(\psi)} = \mathbf{U}_{s,q}^{(\psi)} \left(\left(\mathbf{U}_{s,q}^{(\psi)} \right)^H \mathbf{U}_{s,q}^{(\psi)} \right)^{-1} \left(\mathbf{U}_{s,q}^{(\psi)} \right)^H. \quad (7)$$

The *CSI-capture efficiency* of this subspace is defined as

$$\eta_{s,q}^{(\psi)}(\mathbf{h}_{s,q}) \triangleq \frac{\|\mathbf{P}_{s,q}^{(\psi)} \mathbf{h}_{s,q}\|_2^2}{\|\mathbf{h}_{s,q}\|_2^2}. \quad (8)$$

This ratio is the normalized projection power of $\mathbf{h}_{s,q}$ onto the representing subspace selected by rule ψ . A value close to one means that the selected subspace preserves most of the channel direction, whereas a small value indicates severe channel-power loss before data precoding. When maximum-ratio transmission (MRT) is applied within the selected sub-

¹Current NR systems typically rely on predefined SSB beams, e.g., DFT codebook. However, SSBF studies have shown that this codebook can be optimized w.r.t. the particular propagation environment in a certain site, hence we attach the site index to \mathbf{B}_s to allow site-dependent SSB codebooks [22], [23].

space, the resulting beamforming vector is

$$\hat{\mathbf{w}}_{s,q}^{(\psi)} = \frac{\mathbf{P}_{s,q}^{(\psi)} \mathbf{h}_{s,q}}{\|\mathbf{P}_{s,q}^{(\psi)} \mathbf{h}_{s,q}\|_2}. \quad (9)$$

The corresponding signal-to-noise ratio (SNR) is $\rho_{s,q} \eta_{s,q}^{(\psi)}(\mathbf{h}_{s,q})$, where $\rho_{s,q} \triangleq \frac{P_s \|\mathbf{h}_{s,q}\|_2^2}{\sigma_{n,s}^2}$ denotes the full-CSI SNR. Thus, for a fixed full-CSI SNR, the CSI-capture efficiency directly characterizes the SNR fraction preserved by feedback rule ψ .

C. Problem Formulation

We design the limited feedback system to maximize the achievable data rate while keeping the associated overhead affordable. Accordingly, for UE q in site s , we formulate the feedback design problem for rule ψ as

$$\max_{\psi \in \Psi} R_{s,q}(\psi) = \left(1 - \frac{T_o(\psi)}{T}\right) \log_2 \left(1 + \rho_{s,q} \eta_{s,q}^{(\psi)}(\mathbf{h}_{s,q})\right), \quad (10)$$

where Ψ is the feasible set of feedback rules, $T_o(\psi)$ denotes the channel-use overhead induced by rule ψ , and T is the coherence interval length in channel uses. $T_o(\psi)$ usually consists of SSB/CSI-RS transmission/feedback overheads.

The optimization in (10) couples CSI acquisition quality and signaling overhead through the same feedback rule ψ . In particular, richer measurements may improve the CSI-capture factor $\eta_{s,q}^{(\psi)}(\mathbf{h}_{s,q})$, but they also increase $T_o(\psi)$ and reduce the effective data-transmission time. Since the useful CSI subspace is channel dependent whereas full CSI is unavailable at the BS before feedback, improving (10) requires a prior that links limited measurements to effective subspace decisions. Site-specific learning provides such a prior from target-site samples and is effective when one deployment confines channels to a limited propagation geometry. Scaling this idea to many sites, however, requires repeated labeled-data collection and training over diverse channel distributions, which becomes prohibitive at network scale. Wireless foundation models can address this challenge by learning transferable wireless representations from diverse deployments and adapting them to new sites with limited calibration data.

III. SiFo FOR SITE-SPECIFIC CSI FEEDBACK

In this section, we present the proposed SiFo framework for solving (10). The framework combines the cross-site transfer capability of wireless foundation models with the local propagation adaptation of site-specific learning, thereby providing a data-efficient and low-overhead solution to (10). We first give the preliminary analysis that motivates SiFo, and then describe the proposed framework.

A. Preliminary Analysis

1) *A Joint Analysis of Site-Agnostic and Site-Specific Feedback*: The feedback rule in (10) can use different levels of site information. Conventional NR feedback represents the site-agnostic case, where one standardized codebook and feedback structure are applied to all sites. This rule is fixed before target-site propagation statistics are observed and corresponds to

$$\psi_{\text{agn}}^* = \arg \max_{\psi \in \Psi} \mathbb{E}_s \mathbb{E}_{q|s} [R_{s,q}(\psi)], \quad (11)$$

which maximizes the expected effective spectral efficiency over the population of sites and UEs. Type-I, Type-II, and PSC are representative standardized instantiations of this principle. Detailed analysis of these three schemes is provided in [23]. Among them, Type-II feedback offers the richest subspace representation and highest spectral efficiency, but requires substantial online CSI acquisition, feedback overhead, and UE-side processing.

Site-specific feedback allows the acquisition rule to depend on the deployment site. For a fixed site s , the ideal site-conditioned rule solves

$$\psi_s^* = \arg \max_{\psi \in \Psi} \mathbb{E}_{q|s} [R_{s,q}(\psi)]. \quad (12)$$

The dependence of ψ_s^* on s represents the use of SSI, where the BS exploits target-site propagation statistics rather than applying one common rule to all sites.

It is worth noting that site-agnostic design can be regarded as a special case of site-specific design by setting $\psi_s \equiv \psi$ for all s , leading to the following inequality

$$\mathbb{E}_s \left[\max_{\psi \in \Psi} \mathbb{E}_{q|s} [R_{s,q}(\psi)] \right] \geq \max_{\psi \in \Psi} \mathbb{E}_s \mathbb{E}_{q|s} [R_{s,q}(\psi)]. \quad (13)$$

The inequality quantifies the target pursued by site-specific feedback: local propagation statistics can improve the rate objective by both increasing CSI-capture efficiency and reducing CSI acquisition overhead. Realizing this target requires an accurate site-conditioned rule for each deployment. The key difficulty is how to obtain such rules without collecting a large labeled dataset and retraining model for every new site.

2) *Single-Site SST2 as Site-Specific Feedback*: SST2 can be viewed as a learnable realization of the site-specific design in (12). Instead of requiring the UE to construct a high-resolution Type-II CSI feedback representation, SST2 shifts the subspace inference burden to the BS. Let $\Theta = (\Theta_B, \Theta_H)$ collect the trainable SST2 parameters, where Θ_B parameterizes the probing codebook and Θ_H parameterizes the subspace inference module. An SST2 model can then be written as

$$\psi_{\Theta}^{\text{SST2}} = (\mathbf{B}_{\Theta_B}, H_{\Theta_H}), \quad (14)$$

where \mathbf{B}_{Θ_B} generates a low-dimensional RSRP fingerprint and H_{Θ_H} maps this fingerprint to a representing subspace. When the distinction between the two parameter blocks is not essential, we use the shorthand \mathbf{B}_{Θ} and H_{Θ} . For UE q in site s , following model (5), the measured fingerprint is given by

$$\mathbf{r}_{s,q}(\mathbf{B}_{\Theta}) = \mathcal{M}(\mathbf{h}_{s,q}, \mathbf{B}_{\Theta}) + \mathbf{n}_{s,q}, \quad (15)$$

and the BS predicts the representing subspace as

$$\hat{U}_{s,q} = H_{\Theta}(\mathbf{r}_{s,q}(\mathbf{B}_{\Theta})). \quad (16)$$

Given a prescribed probing budget, the overhead term in (10) is constant across SST2 parameter choices, and the achievable-rate objective becomes monotone in the CSI-capture efficiency. Therefore, the single-site SST2 baseline can be trained through the following capture-efficiency objective:

$$\Theta_s^* = \arg \max_{\Theta} \mathbb{E}_{\mathbf{h} \sim \mathcal{P}_s} [\eta(\mathbf{h}, \psi_{\Theta}^{\text{SST2}})], \quad (17)$$

where \mathcal{P}_s denotes the channel distribution of site s .

This formulation explains why SST2 can be effective. The model only needs to learn the conditional relation induced

by one fixed propagation distribution \mathcal{P}_s rather than to solve a universal RSRP-to-subspace mapping problem. With sufficient data from the same site, SSI supervision resolves the ambiguity between coarse amplitude-only RSRP fingerprints and high-dimensional subspace decisions.

This formulation also exposes the limitation of SST2. The learned parameters in (17) are tied to one deployment distribution. For a new target site t with distribution \mathcal{P}_t , the optimal SST2 parameters may be different:

$$\Theta_t^* = \arg \max_{\Theta} \mathbb{E}_{\mathbf{h} \sim \mathcal{P}_t} [\eta(\mathbf{h}, \psi_{\Theta}^{\text{SST2}})]. \quad (18)$$

Training such a site-specific model from scratch for every target site requires abundant target-site data and repeated training, which limits the scalability of SST2.

3) *Cross-Site Pretraining Limitation*: A natural way to improve scalability is to pretrain one SST2 model over multiple source sites. The corresponding training objective maximizes the average CSI-capture efficiency over the source-site channel distributions:

$$\Theta_0^* = \arg \max_{\Theta} \mathbb{E}_{s \in \mathcal{S}_{\text{src}}} \mathbb{E}_{\mathbf{h} \sim \mathcal{P}_s} [\eta(\mathbf{h}, \psi_{\Theta}^{\text{SST2}})]. \quad (19)$$

This objective produces a single shared SST2 model trained over the source-site mixture. If deployed directly to a new target site, however, the model applies the same rule $\psi_{\Theta_0^*}^{\text{SST2}}$ to all target deployments. Its decision is conditioned on the observed RSRP fingerprint, but not on the local propagation statistics of the target site.

The limitation comes from the ambiguity in inferring CSI subspaces from RSRP fingerprints. For this ambiguity argument, let \mathbf{P}_Q^* denote the full-CSI rank- Q reference projector associated with the prescribed CSI representing subspace, where Q is the representation dimension fixed by the system requirement. For a fixed fingerprint \mathbf{r} , different sites may induce different conditional rank- Q subspace statistics, i.e.,

$$\mathbb{E}[\mathbf{P}_Q^* | \mathbf{r}, s] \neq \mathbb{E}[\mathbf{P}_Q^* | \mathbf{r}, t], \quad (20)$$

because similar amplitude-only RSRP fingerprints can arise from different multipath geometries, angular spreads, phase relations, and scattering structures. Thus, cross-site pretraining can provide a useful marginal prior, but it cannot by itself determine the target-site conditional relation in (20). Limited fine-tuning may partially specialize the parameters, but it still compresses the target-site samples into model weights and does not retain sample-level local evidence during inference.

B. Proposed SiFo Framework

SiFo restores target-site conditioning at inference time. Cross-site pretraining learns a shared SSB probing codebook and a marginal fingerprint-to-subspace prior over source deployments. Target-site calibration then stores local full-CSI subspace evidence as projector-valued memory, so that online UEs can be interpreted relative to calibrated UEs from the same deployment. SiFo operates through three deployment stages as shown in Fig. 1:

- **Stage 1: Cross-site pretraining.** The BS trains an SST2 model on multiple source sites \mathcal{S}_{src} , yielding pretrained parameters Θ_0^* . The resulting model contains a learned probing codebook $\mathbf{B}_{\Theta_0^*}$ and a subspace inference net-

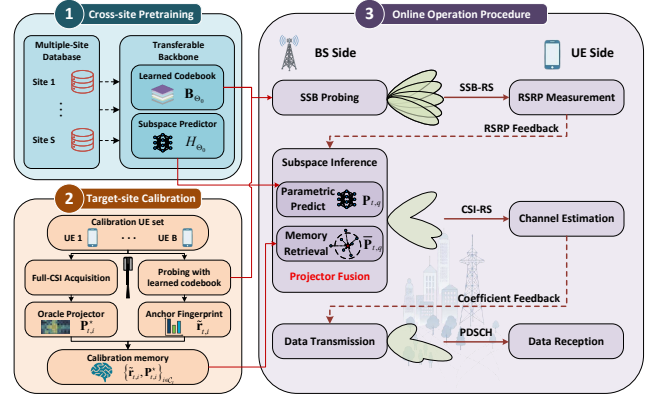


Fig. 1: Illustration of the SiFo framework

work $H_{\Theta_0^*}(\cdot)$ that maps an RSRP fingerprint to a Q -dimensional CSI representation basis. This stage provides shared RSRP fingerprint coordinates and a transferable parametric prior for CSI subspace acquisition.

- **Stage 2: Target-site projector calibration.** For a new target site t , the BS collects a calibration UE set \mathcal{C}_t . Each calibration UE is measured through the pretrained SSB probing codebook and is associated offline with a full-CSI direction projector. These calibrated samples form the target-site projector memory used by the online acquisition rule.
- **Stage 3: Calibration-aided online subspace acquisition.** For served UE q , the UE reports the same K RSRP measurements produced by the pretrained SSB probing codebook. The BS retrieves calibrated UEs with similar fingerprints from the target-site memory, forms a memory-based projector estimate from their full-CSI direction projectors, and fuses it with the parametric subspace prediction through a UE-dependent confidence weight. The fused estimate is then converted into the final CSI representation subspace.

When deployed to a new site, SiFo collects a small size of target-site labels to construct projector memory while the parametric branch remains fixed, i.e., $\Theta_t = \Theta_0^*$. The calibration principle is developed in Section IV. The projector-memory construction and online fusion rule are detailed in Section V. The backbone architecture and deployment implementation are specified in Section VI.

IV. LOW-OVERHEAD TARGET-SITE CALIBRATION

In this section, we develop the low-overhead target-site calibration principle used in Stage 2 of SiFo. The goal is to identify what compact RSRP measurements can provide for Type-II subspace acquisition and why full-CSI-based projector labels are needed during calibration.

A. Calibration RSRP and Directional-Power Statistics

Target-site calibration uses RSRP measurements to sense spatial power over a deployment. The analysis involves two spatial covariance levels: a UE-level covariance for the local CSI representation subspace and a site-level covariance for aggregate directional-power statistics. Throughout this section, channel covariances refer to uncentered spatial second-order

moments. Let $q \sim \mathcal{Q}_t$ denote a UE in target site t , and let $\mathbf{h} \sim \mathcal{P}_t(\cdot|q)$ denote its local downlink channel distribution. The UE-level channel covariance is defined as

$$\mathbf{R}_{t,q}^{\text{UE}} \triangleq \mathbb{E}_{\mathbf{h} \sim \mathcal{P}_t(\cdot|q)} [\mathbf{h}\mathbf{h}^H]. \quad (21)$$

The site-level channel covariance is the mixture of UE-level covariances over the deployment, which is given by

$$\mathbf{R}_t = \mathbb{E}_{q \sim \mathcal{Q}_t} [\mathbf{R}_{t,q}^{\text{UE}}] = \mathbb{E}_{\mathbf{h} \sim \mathcal{P}_t} [\mathbf{h}\mathbf{h}^H]. \quad (22)$$

Here, \mathcal{P}_t denotes the marginal target-site channel distribution. Thus, \mathbf{R}_t describes the aggregate, power-weighted spatial structure sensed over the site, while $\mathbf{R}_{t,q}^{\text{UE}}$ describes the local spatial statistics relevant to UE q .

Under the Type-II feedback budget, the BS ultimately selects a prescribed Q -dimensional CSI representation subspace for each UE. If the UE-level covariance were available, the full-CSI reference subspace for UE q would be the Q -dimensional eigenspace that captures the largest average channel power. Large-scale gain affects the received SNR but not this spatial eigenspace. Therefore, the following normalized UE-level covariance is adopted:

$$\tilde{\mathbf{R}}_{t,q}^{\text{UE}} \triangleq \frac{\mathbf{R}_{t,q}^{\text{UE}}}{\text{tr}(\mathbf{R}_{t,q}^{\text{UE}})}, \quad (23)$$

which preserves the eigenspaces of $\mathbf{R}_{t,q}^{\text{UE}}$ while removing power scaling. The corresponding full-CSI reference subspace is the dominant Q -dimensional eigenspace of $\tilde{\mathbf{R}}_{t,q}^{\text{UE}}$. The site-level covariance \mathbf{R}_t governs directional-power statistics over the deployment, whereas $\tilde{\mathbf{R}}_{t,q}^{\text{UE}}$ determines the local CSI representation subspace for UE q .

Let $\mathbf{S} = [\mathbf{s}_1, \dots, \mathbf{s}_J] \in \mathbb{C}^{N_t \times J}$ denote a generic RSRP sensing codebook. For calibration UE $i \in \mathcal{C}_t$, the noise-free linear-domain RSRP fingerprint induced by \mathbf{S} is

$$\bar{\mathbf{r}}_{t,i}(\mathbf{S}) = [|\mathbf{s}_1^H \mathbf{h}_{t,i}|^2, \dots, |\mathbf{s}_J^H \mathbf{h}_{t,i}|^2]^T = |\mathbf{S}^H \mathbf{h}_{t,i}|^2, \quad (24)$$

where the absolute value and square operations are performed element-wise. The corresponding population directional-power statistic is

$$\boldsymbol{\pi}_t(\mathbf{S}) = \mathbb{E}_{\mathbf{h} \sim \mathcal{P}_t} [|\mathbf{S}^H \mathbf{h}|^2] = \text{diag}(\mathbf{S}^H \mathbf{R}_t \mathbf{S}), \quad (25)$$

whose ℓ -th entry can be expressed as $[\boldsymbol{\pi}_t(\mathbf{S})]_\ell = \mathbf{s}_\ell^H \mathbf{R}_t \mathbf{s}_\ell$. The ℓ -th entry therefore represents the site-average received power along sensing direction \mathbf{s}_ℓ . Thus, calibration RSRP observes diagonal directional-power projections of \mathbf{R}_t in the sensing coordinates. This is the spatial information supplied by RSRP: sample-level beam-power fingerprints and their site-level directional-power statistics.

In SiFo, the generic sensing codebook \mathbf{S} is instantiated by the pretrained learned SSB codebook $\mathbf{B}_{\Theta_0^*}$ for both calibration UEs and online served UEs. Using the same SSB probing codebook places calibration fingerprints and online query fingerprints in the same beam-power coordinate system, so nearest-neighbor retrieval compares responses generated by the same probing beams.

B. Prior-Free Sensing Principle

RSRP sensing observes directional projections of the unknown site-level channel covariance \mathbf{R}_t . If \mathbf{R}_t were available, the sensing beams could be designed to emphasize

the dominant site-specific angular subspace. Before target-site calibration, however, neither \mathcal{P}_t nor \mathbf{R}_t is known to the BS. This motivates a prior-free reference criterion for sensing design: before observing SSI, the sensing codebook should not privilege any site-specific angular sector.

Assumption 2 (*Isotropic sensing prior for unknown sites*). Before SSI is collected, no unit-norm direction in \mathbb{C}^{N_t} is regarded as more likely or more important than any other. The calibration-stage sensing codebook should therefore provide directionally uniform observability and avoid blind spatial directions, rather than optimize for any presumed site-dependent angular sector.

The isotropic prior is epistemic rather than physical: real deployment sites are generally anisotropic once geometry and scatterers are fixed. It only states that, before SSI is observed, the sensing design itself should not encode a site-specific angular preference. For a unit-norm channel direction \mathbf{h} , the sensing energy collected by \mathbf{S} is $\|\mathbf{S}^H \mathbf{h}\|_2^2 = \mathbf{h}^H \mathbf{S} \mathbf{S}^H \mathbf{h}$. Therefore, the prior-free reference design that maximizes the worst-case sensing energy can be formulated into the following optimization problem:

$$\max_{\mathbf{S}} \min_{\|\mathbf{h}\|_2=1} \|\mathbf{S}^H \mathbf{h}\|_2^2 \quad (26a)$$

$$\text{s.t. } \|\mathbf{s}_j\|_2 = 1, \quad j = 1, \dots, J, \quad (26b)$$

$$\mathbf{s}_j \in \mathcal{A}_{\text{RF}}, \quad j = 1, \dots, J, \quad (26c)$$

where the unit-norm constraint fixes the per-beam sensing power, and \mathcal{A}_{RF} captures analog-beam feasibility constraints such as phase-only or quantized-phase implementations.

The sensing-budget consequence follows from the rank of the sensing covariance. With fewer than N_t sensing beams, the rank satisfies

$$\text{rank}(\mathbf{S} \mathbf{S}^H) \leq J < N_t. \quad (27)$$

As a consequence, the sensing beams span at most a J -dimensional subspace of \mathbb{C}^{N_t} . Hence, there exists a unit-norm direction $\mathbf{h}_0 \in \text{span}\{\mathbf{s}_1, \dots, \mathbf{s}_J\}^\perp$ for which $\mathbf{S}^H \mathbf{h}_0 = \mathbf{0}$ and hence

$$\min_{\|\mathbf{h}\|_2=1} \|\mathbf{S}^H \mathbf{h}\|_2^2 = 0. \quad (28)$$

Thus, no prior-free sensing design with fewer than N_t beams can avoid blind spatial directions in the worst case. The case $J = N_t$ is therefore the minimum non-degenerate full-coverage reference, and it is characterized below.

Theorem 1 (*Minimum-budget full-coverage sensing reference*). Consider (26) with $J = N_t$ unit-norm sensing beams. The optimal worst-case sensing energy is one. Moreover, a feasible codebook attains this value if and only if $\mathbf{S} \mathbf{S}^H = \mathbf{I}_{N_t}$. Consequently, any feasible unitary sensing codebook is optimal. For a ULA with N_t antennas, the DFT- N_t codebook $\mathbf{S}^* = \mathbf{D}_{N_t}$ is one such optimal solution, where

$$[\mathbf{D}_{N_t}]_{n,k} = \frac{1}{\sqrt{N_t}} e^{-j \frac{2\pi}{N_t} nk}, \quad n, k = 0, \dots, N_t - 1. \quad (29)$$

Proof: See Appendix A. ■

Remark 1 (*Implication for learned low-overhead probing*). **Theorem 1** gives a prior-free full-coverage reference: at least

N_t beams are needed to avoid blind spatial directions, and the non-redundant solution is orthogonal sensing. The DFT- N_t codebook is one convenient ULA realization, but deploying N_t SSB beams would impose excessive synchronization-stage overhead. SiFo therefore uses a low-dimensional learned codebook with $K \ll N_t$, accepting that worst-case full-space coverage is no longer possible. In this finite-budget regime, the probing beams should remain orthogonal within the selected K -beam sensing subspace and produce distinguishable RSRP angular responses for downstream subspace acquisition. The former is measured by the off-diagonal energy of the Gram matrix of $\mathbf{B}_{\Theta_0^*}$, i.e., $\mathbf{B}_{\Theta_0^*}^H \mathbf{B}_{\Theta_0^*}$. Section VII-D shows that the learned codebook is naturally near-orthogonal and approaches the performance of a wider DFT reference with significantly reduced overhead.

Remark 2 (*Angular interpretation of directional-power sensing*). For a ULA, directional-power sensing admits an angular-kernel interpretation. The DFT reference corresponds to fixed Dirichlet kernels on a uniform angular grid, yielding an angular-bin power profile with leakage and multi-cluster peaks at the UE-sample level. At the site level, the corresponding population statistic is $\text{diag}(\mathbf{D}_{N_t}^H \mathbf{R}_t \mathbf{D}_{N_t})$, which represents a DFT-smoothed angular power spectrum of the target-site covariance. A learned probing codebook replaces the fixed DFT grid with data-adapted directional kernels, so $\text{diag}(\mathbf{B}_{\Theta_0^*}^H \mathbf{R}_t \mathbf{B}_{\Theta_0^*})$ gives the same site-level directional-power statistic measured in the learned sensing coordinates. The SiFo fingerprint is therefore a low-dimensional sample-level realization of these learned directional-power projections.

C. Full-CSI Direction Labels for Calibration

The prior-free reference clarifies the limitation of low-dimensional probing. In SiFo, the deployed codebook $\mathbf{B}_{\Theta_0^*}$ uses $K \ll N_t$ learned beams, so the resulting RSRP vector is a compact directional-power fingerprint rather than an invertible channel observation. Some spatial directions are inevitably blind or weakly observed under a worst-case full-space criterion.

This compact fingerprint remains useful for indexing calibrated UEs. Target-site propagation is spatially structured, so UEs with similar learned-beam power responses tend to share related dominant angular support, angular spread, or local scattering conditions. With the shared learned codebook, calibration and served UEs are measured in the same beam-power coordinates, and nearby calibration samples provide local references for the served UE.

The RSRP coordinate alone does not specify the associated CSI subspace. Even under the N_t -beam DFT reference, RSRP contains only beam-domain magnitudes for an instantaneous channel or diagonal directional-power statistics at the population level. The off-diagonal covariance information needed to determine CSI subspace geometry remains unobserved. SiFo therefore stores calibration samples in a paired form: the RSRP fingerprint provides the directional-power coordinate, while an offline full-CSI direction projector provides the corresponding subspace label. This paired calibration information enables target-site subspace acquisition with low-dimensional learned K -beam online probing.

V. CALIBRATION-AIDED CSI SUBSPACE ACQUISITION

In this section, we develop the calibration-aided CSI subspace acquisition rule used in Stage 3 of SiFo. The target-site calibration output is a set of projector-labeled RSRP fingerprints, which supports online acquisition through three operations: projector-labeled sample construction, local covariance acquisition from neighboring calibrated UEs, and confidence-weighted fusion with the parametric predictor.

A. Projector-Labeled Calibration Memory

The calibration memory preserves the sample-level relation between a low-dimensional RSRP fingerprint and the corresponding full-CSI reference subspace. With the pretrained K -beam SSB codebook $\mathbf{B}_{\Theta_0^*}$, calibration UE i obtains $\mathbf{r}_{t,i}$ following (5). For calibration-neighbor search, the relevant information is the shape of the beam-power response across the learned SSB beams. This shape reflects the UE's angular support, angular spread, and local scattering structure, whereas the total RSRP level is dominated by large-scale gain and does not change the desired subspace. Since the projector label below is also gain-invariant, SiFo uses the normalized RSRP profile as the calibration key, which is given by

$$\tilde{\mathbf{r}}_{t,i} = \frac{\mathbf{r}_{t,i}}{\|\mathbf{r}_{t,i}\|_2} \in \mathbb{R}^{K \times 1}. \quad (30)$$

Because calibration and online UEs are measured by the same probing codebook, their normalized fingerprints are comparable in a common learned beam-power coordinate system.

The RSRP key identifies local similarity under the shared probing codebook, but it is not itself a CSI subspace decision. The calibration memory is hence defined as a set of key-value pairs, where the key is the normalized RSRP profile and the value is the gain-normalized full-CSI direction projector:

$$\mathcal{Y}_t = \{(\tilde{\mathbf{r}}_{t,i}, \mathbf{P}_{t,i}^*)\}_{i \in \mathcal{C}_t}, \quad \mathbf{P}_{t,i}^* = \frac{\mathbf{h}_{t,i} \mathbf{h}_{t,i}^H}{\|\mathbf{h}_{t,i}\|_2^2}. \quad (31)$$

The projector $\mathbf{P}_{t,i}^*$ records the normalized spatial direction observed from the full-CSI vector of calibration UE i . Since one calibration channel vector provides only one spatial direction, this label is a direction-level covariance sample rather than the final rank- Q CSI representation subspace. The prescribed Q -dimensional subspace is formed later by averaging the projectors of neighboring calibrated UEs in (38) and extracting the dominant rank- Q eigenspace in (43). For any candidate precoding vector \mathbf{v} , the quadratic form $\mathbf{v}^H \mathbf{P}_{t,i}^* \mathbf{v}$ measures how much of \mathbf{v} lies along the true channel direction after channel gain and common phase are removed. Hence, $\mathbf{P}_{t,i}^*$ supplies the phase-aware spatial-direction information that the amplitude-only RSRP key $\tilde{\mathbf{r}}_{t,i}$ cannot provide.

Lemma 1 (*Full-CSI direction sample and local covariance*). Under the sparse geometric channel model and **Assumption 1**, further assume that the instantaneous channel power concentrates around its UE-level average, i.e.,

$$\|\mathbf{h}_{t,i}\|_2^2 \approx \mathbb{E}_{\mathbf{h}_{t,i} \sim \mathcal{P}_{t,i}^{\text{UE}}} [\|\mathbf{h}_{t,i}\|_2^2] = \text{tr}(\mathbf{R}_{t,i}^{\text{UE}}), \quad (32)$$

where $\mathcal{P}_{t,i}^{\text{UE}}$ denotes the local channel distribution of calibration UE i . Then the full-CSI direction projector satisfies

$$\mathbb{E}_{\mathbf{h}_{t,i} \sim \mathcal{P}_{t,i}^{\text{UE}}} [\mathbf{P}_{t,i}^*] \approx \tilde{\mathbf{R}}_{t,i}^{\text{UE}}, \quad (33)$$

where $\tilde{\mathbf{R}}_{t,i}^{\text{UE}}$ is defined by (23).

Proof: See Appendix B. ■

Lemma 1 establishes the statistical link between the stored full-CSI direction labels and the local normalized covariance. Each calibration entry therefore provides a phase-aware spatial-direction observation, which becomes informative for Type-II subspace extraction after aggregation over neighboring entries with similar RSRP fingerprints.

B. Local Channel-Covariance Acquisition

For a served UE q in target site t , the BS obtains its normalized RSRP fingerprint $\tilde{\mathbf{r}}_{t,q}$ from SSB probing following (5). The site-average covariance \mathbf{R}_t is coarse for UE-level subspace acquisition because it averages UEs with different angular supports and scattering conditions. The relevant statistic is instead a covariance conditioned on the served UE's normalized RSRP fingerprint, which selects calibration UEs with similar learned-beam power responses. Since large-scale channel power does not change the desired CSI representation subspace, this local statistic is formed after channel-gain normalization. The resulting fingerprint-conditioned local covariance is defined as

$$\mathbf{C}_t(\tilde{\mathbf{r}}_{t,q}) \triangleq \mathbb{E}_{\mathbf{h} \sim \mathcal{P}_t} \left[\frac{\mathbf{h}\mathbf{h}^H}{\|\mathbf{h}\|_2^2} \middle| \tilde{\mathbf{r}}(\mathbf{h}) \simeq \tilde{\mathbf{r}}_{t,q} \right]. \quad (34)$$

The site-level average of these gain-normalized channel directions removes the channel-power weighting retained by \mathbf{R}_t in (22), which is given by

$$\mathbb{E}_{\tilde{\mathbf{r}}} [\mathbf{C}_t(\tilde{\mathbf{r}})] = \mathbb{E}_{\mathbf{h} \sim \mathcal{P}_t} \left[\frac{\mathbf{h}\mathbf{h}^H}{\|\mathbf{h}\|_2^2} \right], \quad (35)$$

Assumption 3 (*Fingerprint-local channel stationarity*). Let $\mathcal{N}(q) \subseteq \mathcal{C}_t$ denote a sufficiently small neighborhood of the served UE q in the normalized RSRP fingerprint space. For any calibration UE $q' \in \mathcal{N}(q)$, the normalized UE-level channel covariance varies slowly within this neighborhood, i.e.,

$$\tilde{\mathbf{R}}_{t,q'}^{\text{UE}} \approx \tilde{\mathbf{R}}_{t,q}^{\text{UE}}. \quad (36)$$

Under **Assumption 3**, the local covariance in (34) has the same dominant subspace as the UE-level normalized covariance, i.e.,

$$\mathbf{C}_t(\tilde{\mathbf{r}}_{t,q}) \approx \tilde{\mathbf{R}}_{t,q}^{\text{UE}}. \quad (37)$$

Let m denote the neighborhood size and $\mathcal{N}_m(q) \subseteq \mathcal{C}_t$ denote the nearest calibration indices to $\tilde{\mathbf{r}}_{t,q}$ by cosine similarity. The local covariance estimate is acquired by averaging their projector labels, which is given by

$$\hat{\mathbf{P}}_{t,q}^{(m)}(\tilde{\mathbf{r}}_{t,q}) = \frac{1}{m} \sum_{i \in \mathcal{N}_m(q)} \mathbf{P}_{t,i}^*. \quad (38)$$

By **Lemma 1**, each term in (38) is a gain-normalized covariance sample. By the local stationarity assumption, neighboring terms correspond to similar local spatial statistics. Therefore, $\hat{\mathbf{P}}_{t,q}^{(m)}(\tilde{\mathbf{r}}_{t,q})$ is an empirical estimate of $\mathbf{C}_t(\tilde{\mathbf{r}}_{t,q})$.

Theorem 2 (*Consistency of local covariance acquisition*). Under **Assumption 3**, consider a sequence of calibration sets with $|\mathcal{C}_t| \rightarrow \infty$ and neighborhood sizes satisfying $m(|\mathcal{C}_t|) \rightarrow \infty$ and $m/|\mathcal{C}_t| \rightarrow 0$. The local projector average in (38)

is then asymptotically unbiased for the UE-level normalized covariance, i.e.,

$$\mathbb{E} \left[\hat{\mathbf{P}}_{t,q}^{(m)}(\tilde{\mathbf{r}}_{t,q}) \right] \xrightarrow{|\mathcal{C}_t| \rightarrow \infty} \tilde{\mathbf{R}}_{t,q}^{\text{UE}}. \quad (39)$$

The same limit holds for any finite average of neighborhood sizes satisfying the same scaling.

Proof: See Appendix C. ■

Theorem 2 formalizes the role of calibration coverage: as calibrated samples become dense in the target-site fingerprint space, projector averaging recovers the local normalized channel covariance associated with the served UE. In finite calibration sets, the neighborhood size controls a variance–locality tradeoff. SiFo therefore averages several neighborhood estimates,

$$\bar{\mathbf{P}}_{t,q}(\tilde{\mathbf{r}}_{t,q}) = \frac{1}{|\mathcal{S}_m|} \sum_{m \in \mathcal{S}_m} \hat{\mathbf{P}}_{t,q}^{(m)}(\tilde{\mathbf{r}}_{t,q}), \quad (40)$$

where \mathcal{S}_m is a finite set of neighborhood sizes specified in Section VII.

C. Confidence-Weighted Fusion and Subspace Extraction

With a finite calibration set, the memory estimate is reliable only when the served UE has close calibrated neighbors in fingerprint space. When no close neighbor exists, the pre-trained SST2 subspace inference network provides a complementary parametric estimate $\tilde{\mathbf{P}}_{t,q}(\mathbf{r}_{t,q}, \boldsymbol{\Theta}_t)$, which represents the cross-site learned subspace prior conditioned on the same RSRP observation. For SiFo deployment, $\boldsymbol{\Theta}_t = \boldsymbol{\Theta}_0^*$. Fine-tuned parameters are used only in the FT-SST2 baseline. The final acquisition rule therefore fuses the parametric and memory estimates through a UE-dependent confidence weight $\alpha_q \in [0, 1]$:

$$\hat{\mathbf{P}}_{t,q}^{\text{mix}} = (1 - \alpha_q) \tilde{\mathbf{P}}_{t,q}(\mathbf{r}_{t,q}, \boldsymbol{\Theta}_t) + \alpha_q \bar{\mathbf{P}}_{t,q}(\tilde{\mathbf{r}}_{t,q}). \quad (41)$$

Although the memory labels are projector-valued, the multi-scale average $\bar{\mathbf{P}}_{t,q}$ and the fused matrix $\hat{\mathbf{P}}_{t,q}^{\text{mix}}$ are covariance estimates before rank reduction. To state the resulting subspace constraint, let

$$\mathcal{P}_Q \triangleq \{ \mathbf{P} : \mathbf{P} = \mathbf{P}^H, \mathbf{P}^2 = \mathbf{P}, \text{rank}(\mathbf{P}) = Q \} \quad (42)$$

denote the set of rank- Q orthogonal projectors. After projector averaging and fusion, $\bar{\mathbf{P}}_{t,q} \notin \mathcal{P}_Q$ and $\hat{\mathbf{P}}_{t,q}^{\text{mix}} \notin \mathcal{P}_Q$ in general: they generally lose idempotence and may have rank larger than Q . Instead, they represent gain-normalized spatial covariance estimates, from which the protocol-constrained rank- Q CSI subspace is extracted. For any Hermitian matrix \mathbf{A} , let $\boldsymbol{\Pi}_Q(\mathbf{A}) \in \mathcal{P}_Q$ denote any projector onto a dominant Q -dimensional eigenspace of \mathbf{A} . Under the prescribed Q -dimensional CSI representing-subspace constraint, the final CSI subspace decision is

$$\hat{\mathbf{P}}_{t,q}^Q \triangleq \boldsymbol{\Pi}_Q(\hat{\mathbf{P}}_{t,q}^{\text{mix}}) = \mathbf{U}_Q \mathbf{U}_Q^H, \quad (43)$$

where the columns of $\mathbf{U}_Q \in \mathbb{C}^{N_t \times Q}$ are the Q eigenvectors of $\hat{\mathbf{P}}_{t,q}^{\text{mix}}$ associated with its Q largest eigenvalues.

Lemma 2 (*Near-reference rank- Q subspace extraction*). Define the UE full-CSI Type-II reference projector as

$$\mathbf{P}_{t,q}^{\text{ref},Q} \triangleq \boldsymbol{\Pi}_Q(\tilde{\mathbf{R}}_{t,q}^{\text{UE}}), \quad (44)$$

which is the rank- Q subspace that would be selected if the UE-level normalized covariance were known. The projector $\hat{\mathbf{P}}_{t,q}^Q$ in (43) satisfies

$$\hat{\mathbf{P}}_{t,q}^Q \in \arg \max_{\mathbf{P} \in \mathcal{P}_Q} \text{tr}(\mathbf{P} \hat{\mathbf{P}}_{t,q}^{\text{mix}}), \quad (45)$$

and equivalently gives the closest element of \mathcal{P}_Q to $\hat{\mathbf{P}}_{t,q}^{\text{mix}}$ in Frobenius norm. Moreover, its full-CSI reference capture-power loss satisfies

$$0 \leq \text{tr} \left[\left(\mathbf{P}_{t,q}^{\text{ref},Q} - \hat{\mathbf{P}}_{t,q}^Q \right) \tilde{\mathbf{R}}_{t,q}^{\text{UE}} \right] \leq 2Q \left\| \hat{\mathbf{P}}_{t,q}^{\text{mix}} - \tilde{\mathbf{R}}_{t,q}^{\text{UE}} \right\|_2. \quad (46)$$

Proof: See Appendix D. ■

Lemma 2 connects the covariance-estimation accuracy of SiFo to the quality of the final CSI subspace decision. The eigenspace extraction in (43) is optimal for the fused covariance estimate, and its loss relative to the UE full-CSI reference subspace is controlled by the deviation between $\hat{\mathbf{P}}_{t,q}^{\text{mix}}$ and $\tilde{\mathbf{R}}_{t,q}^{\text{UE}}$. Consequently, calibration-neighbor averaging and confidence-weighted fusion affect the final subspace through the covariance-estimation error in (46).

VI. PRACTICAL IMPLEMENTATION OF SiFo

The preceding sections establish the calibration principle and the projector-memory acquisition rule. This section specifies the deployment protocol of SiFo, separating offline preparation from online CSI subspace acquisition.

A. Offline Pretraining and Calibration Memory Construction

The offline preparation consists of two components: cross-site pretraining of the SST2 backbone and target-site construction of projector-labeled calibration memory.

Pretrained SST2 backbone: The backbone follows the unified site-specific feedback framework of [23]. It contains a learned SSB probing codebook and a subspace inference network trained jointly through the capture-efficiency objective. Concretely,

Learned SSB probing codebook: $\mathbf{B}_\Theta \in \mathbb{C}^{N_t \times K}$ is a learned beamforming matrix whose columns define the K SSB probing beams. For UE q with channel $\mathbf{h}_{s,q}$, the SSB stage produces the RSRP fingerprint $\mathbf{r}_{s,q}(\mathbf{B}_\Theta)$ following (5). This module implements the sensing map $\mathbf{h}_{s,q} \mapsto \mathbf{r}_{s,q}(\mathbf{B}_\Theta)$ under the prescribed SSB probing budget.

Subspace inference network: $H_\Theta : \mathbb{R}^{K \times 1} \rightarrow \mathbb{C}^{N_t \times Q}$ is a learned inference network whose output defines the Q -dimensional CSI representation subspace. For UE q with RSRP fingerprint $\mathbf{r}_{s,q}(\mathbf{B}_\Theta)$, the BS produces $\hat{\mathbf{U}}_{s,q} = H_\Theta(\mathbf{r}_{s,q}(\mathbf{B}_\Theta))$, and the corresponding subspace estimate is $\hat{\mathcal{U}}_{s,q} = \text{span}(\hat{\mathbf{U}}_{s,q})$. The associated orthogonal projector is

$$\tilde{\mathbf{P}}_{s,q}(\mathbf{r}_{s,q}, \Theta) = \hat{\mathbf{U}}_{s,q} \left(\hat{\mathbf{U}}_{s,q}^H \hat{\mathbf{U}}_{s,q} \right)^{-1} \hat{\mathbf{U}}_{s,q}^H. \quad (47)$$

In implementation, H_Θ is a multi-layer perceptron (MLP).

Target-site calibration memory: After cross-site pretraining, the pretrained probing codebook $\mathbf{B}_{\Theta_0^*}$ is kept fixed for both target-site calibration and online serving. This fixed probing codebook ensures that calibration fingerprints and online query fingerprints are expressed in the same learned-beam coordinates.

For each calibration UE $i \in \mathcal{C}_t$ in target site t , the BS obtains its normalized RSRP key $\tilde{\mathbf{r}}_{t,i}$ under $\mathbf{B}_{\Theta_0^*}$ according to (30). The full-CSI channel of the same UE is used offline to construct the direction projector $\mathbf{P}_{t,i}^*$ in (31). The two quantities are paired to form the calibration memory $\mathcal{Y}_t = \{(\tilde{\mathbf{r}}_{t,i}, \mathbf{P}_{t,i}^*)\}_{i \in \mathcal{C}_t}$, where $|\mathcal{C}_t|$ is the number of target-site calibration UEs.

B. Online CSI Subspace Acquisition

For a served UE q at target site t , the BS first obtains the RSRP fingerprint $\mathbf{r}_{t,q}$ and corresponding normalized fingerprint $\tilde{\mathbf{r}}_{t,q}$ under $\mathbf{B}_{\Theta_0^*}$. SiFo then identifies calibrated UEs whose learned-beam response shapes are closest to that of UE q . Specifically, the cosine similarity between UE q and calibration UE i is

$$c_{q,i} = \tilde{\mathbf{r}}_{t,q}^T \tilde{\mathbf{r}}_{t,i}, \quad i \in \mathcal{C}_t. \quad (48)$$

For a given neighborhood size m , the nearest calibration set is

$$\mathcal{N}_m(q) = \text{Top}_m(\{c_{q,i}\}_{i \in \mathcal{C}_t}), \quad (49)$$

where $\text{Top}_m(\cdot)$ returns the indices of the m largest cosine similarities. Their projector labels are averaged according to (38) and (40), producing the memory covariance estimate $\hat{\mathbf{P}}_{t,q}(\tilde{\mathbf{r}}_{t,q})$.

The parametric branch uses the original SSB observation to generate $\hat{\mathbf{U}}_{t,q} = H_{\Theta_t}(\mathbf{r}_{t,q}(\mathbf{B}_{\Theta_t}))$ and forms $\hat{\mathbf{P}}_{t,q}(\mathbf{r}_{t,q}, \Theta_t)$ from $\hat{\mathbf{U}}_{t,q}$ as in (47). In SiFo, $\Theta_t = \Theta_0^*$. For the fine-tuning baseline, only the subspace inference network is updated while the probing codebook remains fixed so that calibration fingerprints do not need to be remeasured.

The fusion rule in (41) is governed by the memory coefficient α_q , which determines the relative contribution of the cross-site parametric prior and the target-site projector-memory estimate. Since both terms aim to approximate the same local normalized covariance, the desired coefficient is determined by their relative estimation accuracy. To express the retrieval confidence, let $i_q^{(1)}$ denote the nearest calibrated UE in the normalized RSRP fingerprint space and define

$$i_q^{(1)} = \arg \max_{i \in \mathcal{C}_t} c_{q,i}, \quad \kappa_q = \text{clip}(c_{q,i_q^{(1)}}, 0, 1). \quad (50)$$

The following proposition formalizes the ideal fusion coefficient under an mean square error (MSE) criterion.

Proposition 1 (Optimal fusion weight). Let $\tilde{\mathbf{P}}_{t,q}(\mathbf{r}_{t,q}, \Theta_t)$ and $\hat{\mathbf{P}}_{t,q}(\tilde{\mathbf{r}}_{t,q})$ be two estimators of the target local normalized covariance $\tilde{\mathbf{R}}_{t,q}^{\text{UE}}$. Let their Frobenius MSE be σ_{par}^2 and $\sigma_{\text{mem}}^2(q)$, respectively, and assume the two errors are uncorrelated. For the linear fusion form in (41), the MSE-optimal memory coefficient is given by

$$\alpha_q^* = \frac{\sigma_{\text{par}}^2}{\sigma_{\text{par}}^2 + \sigma_{\text{mem}}^2(q)}. \quad (51)$$

If $\sigma_{\text{mem}}^2(q)$ is non-increasing in the retrieval confidence κ_q , then α_q^* is monotone non-decreasing in κ_q .

Proof: See Appendix E. ■

The optimal coefficient in (51) depends on estimator error variances that are unavailable during online deployment. **Proposition 1** nevertheless identifies κ_q as a measurable

TABLE I: Simulation settings

Parameter	Description	Value
f_c	Carrier frequency	3.5GHz
BW	Band Width	10 MHz
N_t	Number of BS antennas	64
K	SSB codebook size	16
d	Antenna spacing	$\lambda/2$
Q	Subspace rank	4
σ_{sh}^2	Log-variance of shadowing	1 dB
S_n	Noise power spectrum density	-170 dBm/Hz
P_t	Transmit Power	40dBm
S_m	Neighborhood size set	{5, 10, 20}
ρ_r	Receiving SNR	10 dB

reliability variable for the memory branch, i.e., under local stationarity, a closer calibrated fingerprint indicates a more accurate local covariance estimate and therefore a larger memory weight. SiFo therefore uses the monotone rule

$$\alpha_q = \kappa_q, \quad (52)$$

which implements the trend directly from the RSRP-domain quantity already computed for neighbor selection. The fused covariance estimate is then converted into the protocol-constrained rank- Q subspace by (43).

C. Online and Offline Overhead

The overhead reduction enabled by SiFo can be understood by considering where different Type-II subspace acquisition schemes place the acquisition burden. Conv-T2 [13] places most of this burden in the online procedure: although no site-specific training is required, the subspace decision relies on CSI-RS refinement, UE-side search, and feedback. SST2 [23] shifts this burden from online UE-side searching and feedback to BS-side inference from K SSB RSRP measurements, thereby substantially reducing CSI-RS transmission and feedback overhead. However, this shift is achieved by training a separate model from a large labeled dataset for each target site. The proposed SiFo keeps the same low-overhead online sensing-and-reporting procedure as SST2, while replacing from-scratch target-site training with reusable cross-site pretraining and a moderate-size projector-labeled calibration memory. *The resulting progression moves the dominant burden from per-UE online acquisition, to per-site model training, and finally to reusable pretraining plus lightweight target-site calibration, reducing the total cost of deploying SST2 at a new site.* The effective-rate impact of this burden shift is evaluated in Section VII-E.

VII. NUMERICAL RESULTS

This section first specifies the simulation setup and evaluation protocol, and then reports the main performance validation of the proposed SiFo.

A. Simulation Setup

Experiments are based on ten DeepMIMO city-scale ray-tracing scenarios [30], including New York (NY), Los Angeles (LA), Chicago (CHI), Houston (HOU), Phoenix (PHX), Philadelphia (PHL), Miami (MIA), San Diego (SD), Dallas (DAL), and San Francisco (SF). Cross-site pretraining uses

leave-one-city-out (LOCO) training: for each target city, the pretrained model is trained on the remaining nine cities and then evaluated on this target city. The main LOCO comparison is reported over all 10 cities, while subsequent ablation studies use SD, the most difficult one as shown in Table II, as the representative city. Each city contributes approximately 20,000 UE realizations over a large outdoor service area in average. The main metric is capture efficiency $\eta = \|\mathbf{P}_Q^{(\psi)} \mathbf{h}\|_2^2 / \|\mathbf{h}\|_2^2$, computed from the dominant Q -dimensional eigenspace returned by acquisition rule ψ . Effective rate is also complemented to demonstrate the better overhead-performance trade-off achieved by the proposed framework. Key simulation parameters are listed in Table I. Unless otherwise stated, simulations are conducted based on these default parameters. In this paper, the number of BS antennas, carrier frequency, bandwidth, antenna spacing, SSB probing budget, and subspace rank are kept identical across deployed sites, so that the evaluation focuses on demonstrating the performance of propagation-domain transfer and target-site calibration efficiency.

Training: The model for backbone pretraining is identical to the setup in [23]. Furthermore, pretraining uses the Adam stochastic gradient optimizer [31] with learning rate 10^{-3} , batch size 512, and 20,000 steps. Fine-tuning uses the same optimizer with L2-SP regularization [32] coefficient $\lambda_{\text{sp}} = 10^{-3}$. Memory and fine-tuning samples are drawn from the same target-site pool, and test evaluation is performed on the remaining held-out UEs.

Baselines: We compare against five reference families. *Conv-T2* is a high-overhead conventional reference, implemented with either a DFT-64 angular basis or an oversampled DFT-256 dictionary with orthogonal matching pursuit (OMP) search at UE. *SST2* is the single-site parametric baseline trained with target-site labeled data. *PT-SST2* is the cross-site pretrained model deployed without any target-site adaptation. *FT-SST2* fine-tunes PT-SST2 with labeled target-site samples and does not use projector memory at inference. *SiFo* denotes the proposed gradient-free target-site specialization with projector-labeled calibration UEs and no target-site fine-tuning. The number attached with the method indicates the number of used samples.

B. Overall CSI Subspace Acquisition Performance

Table II summarizes the LOCO CSI-capture results. Target-site labeled budget B indicates the samples available for both memory restoration and fine-tuning. Conv-T2 DFT-256 is included as a high-overhead capture reference, while SiFo uses only the $K = 16$ RSRP measurements produced by SSB probing online and performs no target-site gradient update. The performance increases consistently with calibration-memory size: SiFo-200 already exceeds SST2-5000 on average (0.8872 vs. 0.8732), SiFo-1000 surpasses the DFT-64 Conv-T2 reference (0.9085 vs. 0.9024), and SiFo-5000 reaches 0.9292, outperforming SST2-Full on average and in nine out of ten cities. These results show that projector-labeled calibration memory uses target-site samples more effectively than retraining a separate parametric RSRP-to-subspace model, while the

TABLE II: LOCO CSI-capture efficiency summary. Underlined values mark the high-overhead Conv-T2 DFT-256 upper reference. Bold values mark the best learning-based result in each city.

Scheme	NY	LA	CHI	HOU	PHX	PHL	MIA	SD	DAL	SF	Avg
Conv-T2-DFT-64	0.8874	0.9004	0.9314	0.8903	0.9287	0.8989	0.9238	0.8761	0.8935	0.8929	0.9024
Conv-T2-DFT-256	<u>0.9656</u>	<u>0.9633</u>	<u>0.9843</u>	<u>0.9688</u>	<u>0.9850</u>	<u>0.9647</u>	<u>0.9848</u>	<u>0.9717</u>	<u>0.9675</u>	<u>0.9594</u>	<u>0.9715</u>
SST2-5000	0.8670	0.8520	0.9593	0.8044	0.9082	0.9090	0.9353	0.7736	0.8555	0.8676	0.8732
SST2-Full	0.9135	0.9068	0.9546	0.8978	0.9486	0.9156	0.9641	0.8745	0.9154	0.9048	0.9196
SiFo-200	0.8647	0.8630	0.9556	0.8631	0.9389	0.9200	0.9357	0.7954	0.8660	0.8698	0.8872
SiFo-500	0.8794	0.8787	0.9608	0.8706	0.9436	0.9268	0.9429	0.8203	0.8786	0.8866	0.8988
SiFo-1000	0.8903	0.8912	0.9652	0.8789	0.9485	0.9316	0.9490	0.8424	0.8891	0.8988	0.9085
SiFo-5000	0.9138	0.9213	0.9735	0.9031	0.9592	0.9408	0.9621	0.8847	0.9179	0.9191	0.9292

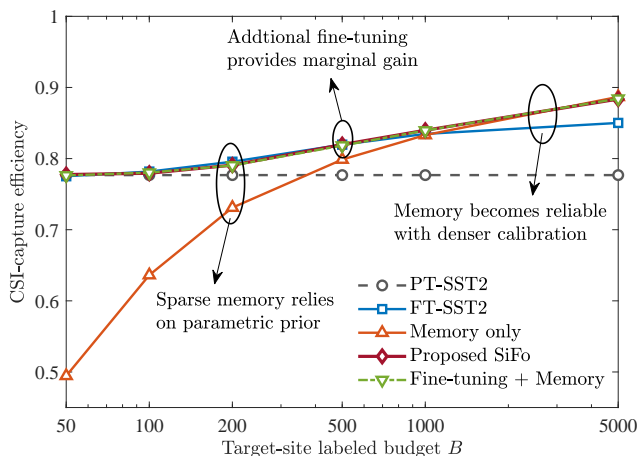


Fig. 2: Comparison of different target-site calibration approaches.

remaining gap to DFT-256 comes with a much lower online sensing and search burden.

C. Impact of Target-Site Calibration

Fig. 2 verifies the complementarity between the parametric and memory branches. The pretrained model gives a stable but site-agnostic prior, while memory-only adaptation uses full-CSI-based projector evidence but becomes unreliable when calibrated neighbors are sparse. The proposed fusion falls back to the parametric prior at small budgets and increasingly exploits projector memory as calibration coverage improves, yielding both cold-start robustness and large-budget gain. Fine-tuning alone remains limited, and adding fine-tuning to memory brings only marginal improvement over the proposed gradient-free rule. This shows that SiFo uses target-site samples more data-efficiently by retaining them as local projector evidence rather than only updating model parameters.

D. Impact of RSRP Sensing Coordinates

Fig. 3 isolates the role of the pretrained sensing coordinates. Random $K = 16$ beams provide weak retrieval geometry, and the fixed DFT-16 grid is limited by its coarse angular resolution. The learned $K = 16$ key consistently improves over DFT-16 at moderate and large calibration budgets, showing that cross-site pretraining shapes the RSRP fingerprint space

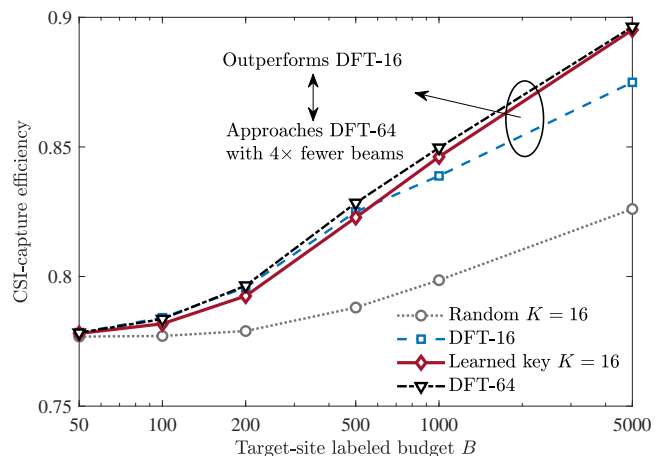


Fig. 3: Comparison of different RSRP sensing coordinates.

for target-site neighbor search rather than merely learning a parametric predictor. It also approaches the DFT-64 reference while using four times fewer probing beams, supporting the low-overhead sensing principle in Remark 1.

We further examine the mutual coherence of the learned beams. For a column-normalized codebook $\mathbf{B} = [\mathbf{b}_1, \dots, \mathbf{b}_K]$, define the average off-diagonal Gram energy as

$$\bar{\mu}_G(\mathbf{B}) = \frac{1}{K(K-1)} \sum_{i \neq j} |\mathbf{b}_i^H \mathbf{b}_j|^2. \quad (53)$$

For the SD LOCO simulation, the learned $K = 16$ probing codebook gives $\bar{\mu}_G(\mathbf{B}_{\Theta_0}) = 0.0132$, indicating low average inter-beam correlation and no evident collapse to repeated beam measurements. This confirms the near-orthogonality aspect of the finite-budget probing principle discussed in Remark 1.

E. Effective Spectral Efficiency Under Limited Target-Site Data

Fig. 4 evaluates whether the CSI-capture gain translates into overhead-aware throughput. Conv-T2 is penalized by CSI-RS and feedback overhead, whereas SST2 and SiFo use the same low-overhead SSB probing and RSRP reporting procedure. Under this accounting, SST2 needs a larger target-site labeled set before surpassing the conventional Type-II references. SiFo crosses these references with fewer target-site samples

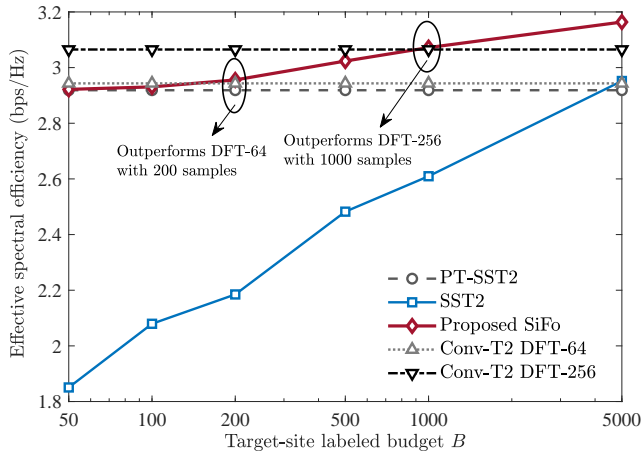


Fig. 4: Effective spectral efficiency comparison under limited target-site data.

because projector memory uses calibration data as local spatial evidence rather than only as training samples for a parametric mapping. This confirms that the data efficiency of SiFo also appears in effective spectral efficiency under practical online overhead.

VIII. CONCLUSION

This paper developed SiFo, a wireless foundation model framework for low-overhead site-specific CSI feedback. The proposed framework combines cross-site pretraining with target-site projector memory. Concretely, the pretrained backbone provides a transferable SSB probing codebook and parametric subspace prior, while calibration memory supplies local full-CSI-based projector evidence for gradient-free target-site specialization. The analysis clarified why RSRP-only sensing cannot specify the phase-aware Type-II subspace, how rank-one full-CSI direction projectors serve as normalized covariance samples, and how neighbor projector averaging and confidence-weighted fusion recover a protocol-constrained rank- Q subspace. Simulations over city-scale deployments showed that SiFo achieves strong CSI-capture performance with substantially lower online overhead than conventional Type-II feedback, uses target-site labeled samples more efficiently than single-site training or fine-tuning-only adaptation, and converts this gain into higher effective spectral efficiency under limited target-site data. These results indicate that foundation model pretraining and projector-labeled calibration memory provide a practical route toward data-efficient and low-overhead site-specific CSI feedback. Future work may extend the framework to online memory updates and broader cross-site adaptation settings.

APPENDIX A PROOF OF THEOREM 1

The minimum collected sensing energy can be obtained via the Rayleigh-Ritz theorem as

$$\min_{\|\mathbf{h}\|_2=1} \|\mathbf{S}^H \mathbf{h}\|_2^2 = \lambda_{\min}(\mathbf{S}\mathbf{S}^H). \quad (54)$$

Since $J = N_t$ and all sensing beams have unit norm, $\text{tr}(\mathbf{S}\mathbf{S}^H) = \text{tr}(\mathbf{S}^H \mathbf{S}) = N_t$. Thus, the average eigenvalue

of $\mathbf{S}\mathbf{S}^H$ is one, which implies $\lambda_{\min}(\mathbf{S}\mathbf{S}^H) \leq 1$. Hence, the optimal worst-case sensing energy is at most one.

Equality holds if and only if all eigenvalues of $\mathbf{S}\mathbf{S}^H$ are equal to one, because their average is one and their minimum is one. This is equivalent to $\mathbf{S}\mathbf{S}^H = \mathbf{I}_{N_t}$. Conversely, any feasible \mathbf{S} satisfying this condition yields $\|\mathbf{S}^H \mathbf{h}\|_2^2 = \mathbf{h}^H \mathbf{h} = 1$ for every unit-norm \mathbf{h} , and therefore attains the upper bound.

Finally, the DFT- N_t codebook is unitary, i.e., $\mathbf{D}_{N_t} \mathbf{D}_{N_t}^H = \mathbf{I}_{N_t}$. It therefore satisfies $\mathbf{S}\mathbf{S}^H = \mathbf{I}_{N_t}$. Its entries also have constant modulus, so it is compatible with the standard phase-only analog beam constraint. The proof is thus completed.

APPENDIX B PROOF OF LEMMA 1

Under path independence and the approximate orthogonality of steering vectors in **Assumption 1**, the following results hold for each channel vector:

$$\mathbf{h}_{t,i} \mathbf{h}_{t,i}^H \approx \sum_{\ell} |\alpha_{t,i,\ell}|^2 \mathbf{a}(u_{t,i,\ell}) \mathbf{a}^H(u_{t,i,\ell}). \quad (55)$$

The corresponding channel power satisfies $\|\mathbf{h}_{t,i}\|_2^2 \approx \sum_{\ell} |\alpha_{t,i,\ell}|^2$. Under the path-power concentration assumption, $\|\mathbf{h}_{t,i}\|_2^2 \approx \text{tr}(\mathbf{R}_{t,i}^{\text{UE}})$ with high probability. Taking expectations and applying this concentration approximation to the denominator gives

$$\mathbb{E} \left[\frac{\mathbf{h}_{t,i} \mathbf{h}_{t,i}^H}{\|\mathbf{h}_{t,i}\|_2^2} \right] \approx \frac{\sum_{\ell} \mathbb{E}[|\alpha_{t,i,\ell}|^2] \mathbf{a}(u_{t,i,\ell}) \mathbf{a}^H(u_{t,i,\ell})}{\text{tr}(\mathbf{R}_{t,i}^{\text{UE}})}. \quad (56)$$

Since the numerator is $\mathbf{R}_{t,i}^{\text{UE}}$ under the same channel model, we have

$$\mathbb{E} \left[\frac{\mathbf{h}_{t,i} \mathbf{h}_{t,i}^H}{\|\mathbf{h}_{t,i}\|_2^2} \right] \approx \frac{\mathbf{R}_{t,i}^{\text{UE}}}{\text{tr}(\mathbf{R}_{t,i}^{\text{UE}})} = \tilde{\mathbf{R}}_{t,i}^{\text{UE}}. \quad (57)$$

In the deterministic path-power case $|\alpha_{t,i,\ell}|^2 \equiv \bar{\sigma}_{t,i,\ell}^2$, the above approximation becomes exact under the near-orthogonal angular model. The proof is thus completed.

APPENDIX C PROOF OF THEOREM 2

As $|\mathcal{C}_t| \rightarrow \infty$ with $m \rightarrow \infty$ and $m/|\mathcal{C}_t| \rightarrow 0$, each nearest-neighbor neighborhood radius in the normalized RSRP fingerprint space shrinks to zero while the number of averaged neighbors grows. By **Assumption 3**, all neighbors in the shrinking neighborhood share the same normalized UE-level covariance in the limit, i.e., $\tilde{\mathbf{R}}_{t,i}^{\text{UE}} \rightarrow \tilde{\mathbf{R}}_{t,q}^{\text{UE}}$. Applying **Lemma 1** to each full-CSI direction projector and then the law of large numbers to the growing average yields

$$\mathbb{E} \left[\hat{\mathbf{P}}_{t,q}^{(m)}(\tilde{\mathbf{r}}_{t,q}) \right] \xrightarrow{|\mathcal{C}_t| \rightarrow \infty} \tilde{\mathbf{R}}_{t,q}^{\text{UE}}. \quad (58)$$

A finite average of several neighborhood estimators with the same limit has the same limit, which proves the multi-scale statement. The proof is thus completed.

APPENDIX D PROOF OF LEMMA 2

Let $\mathbf{T}_q = \tilde{\mathbf{R}}_{t,q}^{\text{UE}}$, $\mathbf{A}_q = \hat{\mathbf{P}}_{t,q}^{\text{mix}}$, and $\mathbf{E}_q = \mathbf{A}_q - \mathbf{T}_q$. Since \mathbf{A}_q is Hermitian, the Ky Fan maximum principle [33] gives

$$\Pi_Q(\mathbf{A}_q) \in \arg \max_{\mathbf{P} \in \mathcal{P}_Q} \text{tr}(\mathbf{P}\mathbf{A}_q), \quad (59)$$

which proves (45). For any $\mathbf{P} \in \mathcal{P}_Q$, $\mathbf{P}^2 = \mathbf{P}$ and $\text{tr}(\mathbf{P}) = Q$, so maximizing $\text{tr}(\mathbf{P}\mathbf{A}_q)$ is equivalent to minimizing $\|\mathbf{A}_q - \mathbf{P}\|_F^2 = \|\mathbf{A}_q\|_F^2 + Q - 2\text{tr}(\mathbf{P}\mathbf{A}_q)$ over \mathcal{P}_Q .

Define

$$\mathcal{L}_q = \text{tr} \left[\left(\mathbf{P}_{t,q}^{\text{ref},Q} - \hat{\mathbf{P}}_{t,q}^Q \right) \mathbf{T}_q \right]. \quad (60)$$

Since $\mathbf{P}_{t,q}^{\text{ref},Q}$ maximizes $\text{tr}(\mathbf{P}\mathbf{T}_q)$ over \mathcal{P}_Q , $\mathcal{L}_q \geq 0$. Moreover, because $\hat{\mathbf{P}}_{t,q}^Q$ maximizes $\text{tr}(\mathbf{P}\mathbf{A}_q)$ over \mathcal{P}_Q ,

$$\mathcal{L}_q = \text{tr} \left[\left(\mathbf{P}_{t,q}^{\text{ref},Q} - \hat{\mathbf{P}}_{t,q}^Q \right) \mathbf{A}_q \right] - \text{tr} \left[\left(\mathbf{P}_{t,q}^{\text{ref},Q} - \hat{\mathbf{P}}_{t,q}^Q \right) \mathbf{E}_q \right] \quad (61)$$

$$\leq \left| \text{tr} \left[\left(\mathbf{P}_{t,q}^{\text{ref},Q} - \hat{\mathbf{P}}_{t,q}^Q \right) \mathbf{E}_q \right] \right|. \quad (62)$$

By trace duality between the nuclear norm and the spectral norm,

$$\mathcal{L}_q \leq \left\| \mathbf{P}_{t,q}^{\text{ref},Q} - \hat{\mathbf{P}}_{t,q}^Q \right\|_* \|\mathbf{E}_q\|_2 \leq 2Q \|\mathbf{E}_q\|_2, \quad (63)$$

because both projectors have nuclear norm Q . The proof is thus completed.

APPENDIX E

PROOF OF PROPOSITION 1

Under uncorrelated estimator errors, the cross-covariance term vanishes. The Frobenius MSE of $\hat{\mathbf{P}}_{t,q}^{\text{mix}} = (1 - \alpha)\tilde{\mathbf{P}}_{t,q}(\mathbf{r}_{t,q}, \boldsymbol{\Theta}_t) + \alpha\hat{\mathbf{P}}_{t,q}(\tilde{\mathbf{r}}_{t,q})$ with respect to $\mathbf{R}_{t,q}^{\text{UE}}$ is $(1 - \alpha)^2\sigma_{\text{par}}^2 + \alpha^2\sigma_{\text{mem}}^2(q)$. This is a convex quadratic in α . Setting its derivative to zero gives $\alpha_q^* = \frac{\sigma_{\text{par}}^2}{\sigma_{\text{par}}^2 + \sigma_{\text{mem}}^2(q)}$. If $\sigma_{\text{mem}}^2(q)$ is non-increasing in κ_q , then α_q^* is non-decreasing in κ_q because α_q^* is a decreasing function of $\sigma_{\text{mem}}^2(q)$. The proof is thus completed.

REFERENCES

- [1] R. Bommasani *et al.*, "On the opportunities and risks of foundation models," *arXiv preprint arXiv:2108.07258*, 2021.
- [2] J. Shao, J. Tong, Q. Wu, W. Guo, Z. Li, Z. Lin, and J. Zhang, "WirelessLLM: Empowering large language models towards wireless intelligence," *J. Commun. Inf. Netw.*, vol. 9, no. 2, pp. 99–112, Jun. 2024.
- [3] B. Liu, S. Gao, X. Liu, X. Cheng, and L. Yang, "WiFo: Wireless foundation model for channel prediction," *Sci. China Inf. Sci.*, vol. 68, no. 6, p. 162302, May 2025.
- [4] S. Alikhani, G. Charan, and A. Alkhateeb, "Large wireless model: Foundation model for wireless channels," *arXiv preprint arXiv:2411.08872*, 2024.
- [5] T. Yang, P. Zhang, M. Zheng, Y. Shi, L. Jing, J. Huang, and N. Li, "WirelessGPT: A generative pre-trained multi-task learning framework for wireless communication and sensing," *IEEE Netw.*, vol. 39, no. 5, pp. 58–65, 2025.
- [6] Y. Sheng, J. Wang, X. Zhou, L. Liang, H. Ye, S. Jin, and G. Y. Li, "A wireless foundation model for multi-task prediction," *arXiv preprint arXiv:2507.05938*, 2025.
- [7] A. Aboufotouh, E. Mohammed, and H. Abou-Zeid, "6G WavesFM: A multimodal foundation model for sensing, communication, and localization," *IEEE Open J. Commun. Soc.*, vol. 6, pp. 6792–6807, 2025.
- [8] F. Zhou, C. Liu, H. Zhang, W. Wu, Q. Wu, T. Q. S. Quek, and C.-B. Chae, "SpectrumFM: A foundation model for intelligent spectrum management," *IEEE J. Sel. Areas Commun.*, vol. 44, no. 2, pp. 4471–4488, 2026.
- [9] O. A. Mashaal and H. Abou-Zeid, "IQFM: A foundation model for wireless multi-antenna IQ streams," *IEEE Open J. Commun. Soc.*, vol. 7, pp. 3483–3501, 2026.
- [10] X. Liu, S. Gao, B. Liu, X. Cheng, and L. Yang, "WiFo-CF: Wireless foundation model for CSI feedback," *IEEE Trans. Wireless Commun.*, vol. 25, pp. 15 039–15 053, 2026.
- [11] D. J. Love, R. W. Heath, V. K. N. Lau, D. Gesbert, B. D. Rao, and M. Andrews, "An overview of limited feedback in wireless communication systems," *IEEE J. Sel. Areas Commun.*, vol. 26, no. 8, pp. 1341–1365, Oct. 2008.
- [12] X. Fu, D. Le Ruyet, R. Visoz, V. Ramireddy, M. Grossmann, M. Landmann, and W. Quiroga, "A tutorial on downlink precoder selection strategies for 3GPP MIMO codebooks," *IEEE Access*, vol. 11, pp. 138 897–138 922, Dec. 2023.
- [13] 3GPP, "NR; physical layer procedures for data," 3rd Generation Partnership Project (3GPP), Technical Specification TS 38.214, 2018.
- [14] R. M. Dreifuerst and R. W. Heath, "Machine learning codebook design for initial access and CSI type-II feedback in sub-6-GHz 5G NR," *IEEE Trans. Wireless Commun.*, vol. 23, no. 6, pp. 6411–6424, Jun. 2024.
- [15] —, "Neural codebook design for MIMO network beam management," *IEEE Trans. Wireless Commun.*, vol. 24, no. 5, pp. 3909–3922, May 2025.
- [16] Y. Heng, J. Mo, and J. G. Andrews, "Learning site-specific probing beams for fast mmwave beam alignment," *IEEE Trans. Wireless Commun.*, vol. 21, no. 8, pp. 5785–5800, Jan. 2022.
- [17] X. Ning, S. Zhang, Y. Xue, X. Zheng, Q. Shi, and T.-H. Chang, "Learning beams adaptive to the environment: An RSRP-based codebook design," in *Proc. IEEE Int. Workshop Signal Process. Adv. Wireless Commun. (SPAWC)*, 2023, pp. 521–525.
- [18] D. Wu, Y. Zeng, S. Jin, and R. Zhang, "Environment-aware hybrid beamforming by leveraging channel knowledge map," *IEEE Trans. Wireless Commun.*, vol. 23, no. 5, pp. 4990–5005, Oct. 2024.
- [19] Y. Zeng, J. Chen, J. Xu, D. Wu, X. Xu, S. Jin, X. Gao, D. Gesbert, S. Cui, and R. Zhang, "A tutorial on environment-aware communications via channel knowledge map for 6g," *IEEE Commun. Surv. Tutorials*, vol. 26, no. 3, pp. 1478–1519, Feb 2024.
- [20] Y. Heng and J. G. Andrews, "Grid-free MIMO beam alignment through site-specific deep learning," *IEEE Trans. Wireless Commun.*, vol. 23, no. 2, pp. 908–921, Feb. 2024.
- [21] Z. Wang, Z. Zhou, C.-J. Zhao, and Y. Liu, "Generative site-specific beamforming for next-generation spatial intelligence," *arXiv preprint arXiv:2601.02301*, 2026.
- [22] C.-J. Zhao, Z. Wang, and Y. Liu, "Generative site-specific beamforming via information-maximizing codebook," *arXiv preprint arXiv:2602.12552*, 2026.
- [23] C.-J. Zhao, Z. Wang, Z. Zhao, and Y. Liu, "Bridging standardized codebook and site-specific beamforming: A unified limited-feedback framework," 2026, manuscript.
- [24] O. E. Ayach, S. Rajagopal, S. Abu-Surra, Z. Pi, and R. W. Heath, "Spatially sparse precoding in millimeter wave MIMO systems," *IEEE Trans. Wireless Commun.*, vol. 13, no. 3, pp. 1499–1513, Mar. 2014.
- [25] H. Q. Ngo, E. G. Larsson, and T. L. Marzetta, "Aspects of favorable propagation in massive MIMO," in *Proc. 22nd Eur. Signal Process. Conf. (EUSIPCO)*, 2014, pp. 76–80.
- [26] E. G. Larsson, O. Edfors, F. Tufvesson, and T. L. Marzetta, "Massive MIMO for next generation wireless systems," *IEEE Commun. Mag.*, vol. 52, no. 2, pp. 186–195, Feb. 2014.
- [27] 3GPP, "NR; physical channels and modulation," 3rd Generation Partnership Project (3GPP), Technical Specification TS 38.211, 2018.
- [28] —, "NR; physical layer measurements," 3rd Generation Partnership Project (3GPP), Technical Specification TS 38.215, 2018.
- [29] M. Giordani, M. Polese, A. Roy, D. Castor, and M. Zorzi, "A tutorial on beam management for 3GPP NR at mmwave frequencies," *IEEE Commun. Surv. Tutorials*, vol. 21, no. 1, pp. 173–196, Sep. 2019.
- [30] A. Alkhateeb, "DeepMIMO: A generic deep learning dataset for millimeter wave and massive MIMO applications," in *Proc. Inf. Theory Appl. Workshop (ITA)*, San Diego, CA, Feb. 2019, pp. 1–8.
- [31] D. P. Kingma and J. Ba, "Adam: A method for stochastic optimization," in *Proc. Int. Conf. Learn. Represent. (ICLR)*, 2015.
- [32] X. Li, Y. Grandvalet, and F. Davoine, "Explicit inductive bias for transfer learning with convolutional networks," in *Proc. Int. Conf. Mach. Learn. (ICML)*, 2018, pp. 2825–2834.
- [33] R. A. Horn and C. R. Johnson, *Matrix Analysis*, 2nd ed. Cambridge University Press, 2012.